LETTER

doi:10.1038/nature11601

# Nonlinear dendritic integration of sensory and motor input during an active sensing task

Ning-long Xu[1], Mark T. Harnett[1], Stephen R. Williams[2], Daniel Huber[1]†, Daniel H. O'Connor[1]†, Karel Svoboda[1] & Jeffrey C. Magee[1]

**Active dendrites provide neurons with powerful processing capabilities. However, little is known about the role of neuronal dendrites in behaviourally related circuit computations. Here we report that a novel global dendritic nonlinearity is involved in the integration of sensory and motor information within layer 5 pyramidal neurons during an active sensing behaviour. Layer 5 pyramidal neurons possess elaborate dendritic arborizations that receive functionally distinct inputs, each targeted to spatially separate regions[1,2]. At the cellular level, coincident input from these segregated pathways initiates regenerative dendritic electrical events that produce bursts of action potential output[3,4] and circuits featuring this powerful dendritic nonlinearity can implement computations based on input correlation[5]. To examine this *in vivo* we recorded dendritic activity in layer 5 pyramidal neurons in the barrel cortex using two-photon calcium imaging in mice performing an object-localization task. Large-amplitude, global calcium signals were observed throughout the apical tuft dendrites when active touch occurred at particular object locations or whisker angles. Such global calcium signals are produced by dendritic plateau potentials that require both vibrissal sensory input and primary motor cortex activity. These data provide direct evidence of nonlinear dendritic processing of correlated sensory and motor information in the mammalian neocortex during active sensation.**

The unique integrative properties of cortical pyramidal neurons enable them to powerfully transform synaptic-input patterns delivered through structured network connectivity[6]. Of particular interest is the ability of pyramidal-neuron dendrites to actively integrate input from spatially segregated and functionally distinct pathways (for example, sensory or motor pathways) when strong temporal correlations exist between these representations[3–5]. Circuit computations based on active dendritic transformation of different streams of information by pyramidal neurons could underlie a variety of functions that include top-down cortical interactions, associative feature binding and predictive coding[5–10]. To investigate the role of dendritic integration in behaviourally relevant network computations, we used two-photon microscopy to image dendritic $Ca^{2+}$ signals from distal tuft branches of layer 5 pyramidal neurons of the barrel cortex (S1) labelled with a genetically encoded calcium indicator (GCaMP3)[11] through a chronic imaging window while mice performed a task based on vibrissal active touch (Fig. 1a and Methods). Head-fixed mice were trained to move either one row of whiskers or a single whisker to locate an object (Fig. 1a, d, Supplementary Fig. 1 and Methods)[12]. In 'go' trials, a vertical pole was presented at one of four positions along the anterior–posterior axis and a correct response was defined as licking for water reward. In 'no-go' trials, the pole was located in a more anterior position and the correct response was to withhold licking. Trained mice touched the pole in the go positions but rarely in the no-go position. Experimental behavioural sessions began after an training period (signal detection statistic (d′) $> 1.8$; Supplementary Fig. 1 and Methods). Whiskers were tracked simultaneously using a high-speed imaging system to quantify whisker-related behavioural variables[13] (Fig. 1a).

During task performance large-amplitude $Ca^{2+}$ transients were observed in apical tuft dendrites of layer 5 pyramidal neurons (~20–200 μm below the pial surface; amplitude, $89.9 \pm 42.9\%$ peak $\Delta F/F$; duration, full width at half maximum $= 0.48 \pm 0.31$ s; Fig. 1b, c, Supplementary Fig. 2 and Methods). The dendritic $Ca^{2+}$ signals were primarily observed during the time period when the target pole was present (sampling period; Fig. 1c, d), and less frequently following this period (post-sampling period; Supplementary Fig. 3 and Methods). Quantitative analysis of the whisker–object interactions showed that dendritic $Ca^{2+}$ transients preferentially occurred in trials that contained whisker–object contacts (Fig. 1c–e), with short latency after first touch ($40 \pm 38$ ms, $n = 57$ regions of interest (ROIs) from 4 animals; Fig. 1d). Periods of isolated whisking (non-touch trials) were not associated with detectable tuft $Ca^{2+}$ transients, even though whisking alone is capable of evoking action potentials in layer 5 pyramidal neurons[14–16]. The touch dependence and short latency from object contact suggest a role for ascending sensory input in the generation of dendritic $Ca^{2+}$ signals. However, passive whisker deflection in anaesthetized mice was ineffective in producing dendritic activation (Supplementary Fig. 4)[17]. The above data suggest that active sensation, involving both whisking and object touch, is required for apical tuft dendrite activation.

To examine the spatial extent of behaviourally evoked dendritic $Ca^{2+}$ signals, we imaged multiple apical dendritic branches of a single neuron simultaneously during behavioural sessions (sparse labelling condition, Fig. 2a and Methods). Large $Ca^{2+}$ signals occurred synchronously in all of the imaged branches belonging to the same cell (Fig. 2b, c), such that strong correlations were observed among the branch $Ca^{2+}$ signals (Fig. 2d, f; $R = 0.69 \pm 0.13$ ($\pm$ s.d.), $n = 18$ neurons; Supplementary Fig. 5). However, this was not the case for branches that belonged to different cells (Fig. 2d–f; $R = 0.097 \pm 0.13$, $n = 30$ imaging fields; Supplementary Fig. 5 and Methods). These results indicate that, in contrast to previous experiments using passive sensory stimulation in anaesthetized mice[17–20] or freely whisking mice[22], a salient behavioural event (that is, active touch) produces a strong activation of the entire apical tuft dendrite region. The widespread nature of the $Ca^{2+}$ signals also differs from that expected from more localized NMDA (*N*-methyl-D-aspartate) spikes[22].

To determine the electrophysiological basis of the observed tuft $Ca^{2+}$ signals, we performed *in vivo* targeted whole-cell recordings from apical tuft dendritic branches of layer 5 pyramidal neurons positive for GCaMP3 in the barrel cortex of anaesthetized mice (Fig. 3a, b). We observed electrical events of moderate amplitude (~30 mV) and relatively long durations (~20 ms) during periods of heightened network activity ('unpaired events', $0.26 \pm 0.13$ Hz; Fig. 3c, d and Supplementary Fig. 6). These unpaired events were not associated with any detectable change in GCaMP3 fluorescence in dendritic regions near the recording pipette (Fig. 3c, d, f). However, prolonged depolarization of the apical tuft dendrite (>15 mV, 500 ms) by current injection converted these electrical events into large-amplitude and long-duration regenerative plateau potentials ('paired events',

[1]Howard Hughes Medical Institute, Janelia Farm Research Campus, Ashburn, Virginia 20147, USA. [2]Queensland Brain Institute, The University of Queensland, St Lucia, Queensland 4072, Australia.
†Present addresses: Department of Basic Neurosciences, University of Geneva, CH-1211 Geneva, Switzerland (D.H.); Department of Neuroscience, Johns Hopkins University School of Medicine, Baltimore, Maryland 21205, USA (D.H.O.).

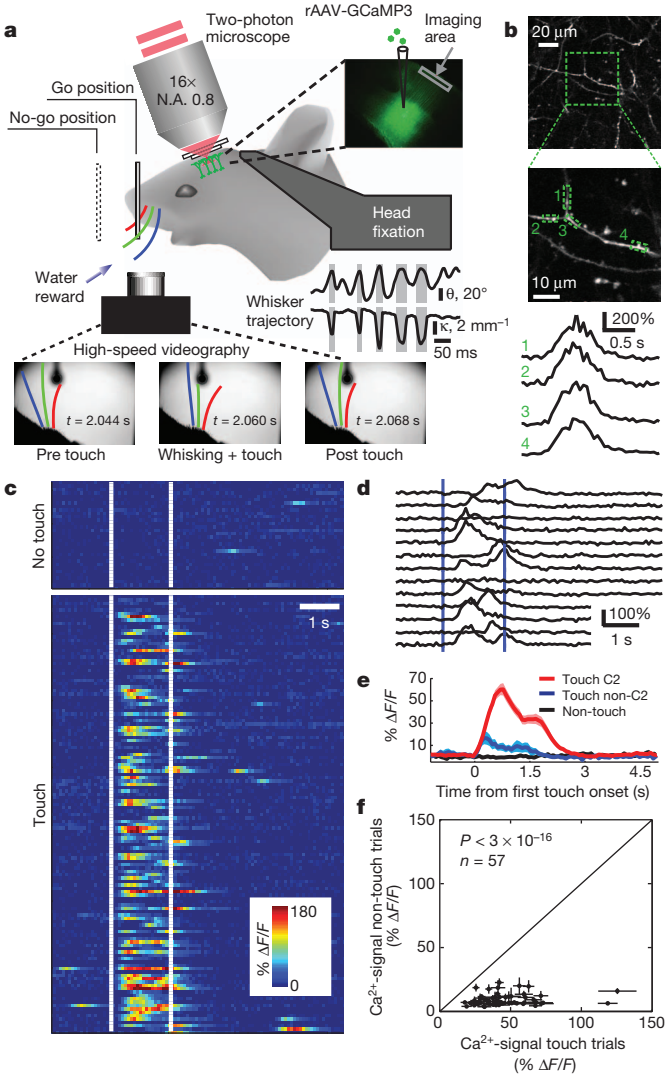


**Figure 1 | Active touch evoked large dendritic $Ca^{2+}$ signals in distal tuft branches of layer 5 pyramids.** **a**, The experimental set-up; a head-fixed mouse performs a whisker-dependent object-localization task under a microscope. The scanning laser beam (red) is focused on distal dendrites of GCaMP3-labelled neurons (green) through an imaging window. The mouse actively whisks to find the pole and makes a lick response (go) or withholds licking (no-go). Whisker motion was recorded (bottom) and quantified (whisker angle, θ, and curvature change, κ; grey shows touch). Top left, schematic showing two-photon imaging set-up. Top right, GCaMP3 is expressed in deep layers of barrel cortex. N.A., numerical aperture. **b**, Tuft branches (top and middle panels) and $Ca^{2+}$ signals ($\Delta F/F$; bottom panel) from different sub-regions of a single branch (green dashed boxes). Middle panel is a magnified version of a region of the top panel (outlined by the green box). **c**, Colour raster of $Ca^{2+}$ signals from all trials of a behavioural session sorted into touch (bottom panel) and non-touch trials (top panel). **d**, Touch trials from **c** expanded as traces. Vertical bars in **c** and **d** show sampling period. **e**, Averaged dendritic $Ca^{2+}$ signals aligned to the onset of touch from trials with C2 whisker touch (Touch C2), with touch from whiskers other than C2 (Touch non-C2) and with no touch (Non-touch). **f**, Population data of dendritic $Ca^{2+}$ signals ($\Delta F/F$ amplitude) during whisker sampling time, compared between touch trials and non-touch trials ($n = 57$ dendritic branches, 4 animals). Data in **e** and **f** are mean ± s.e.m.

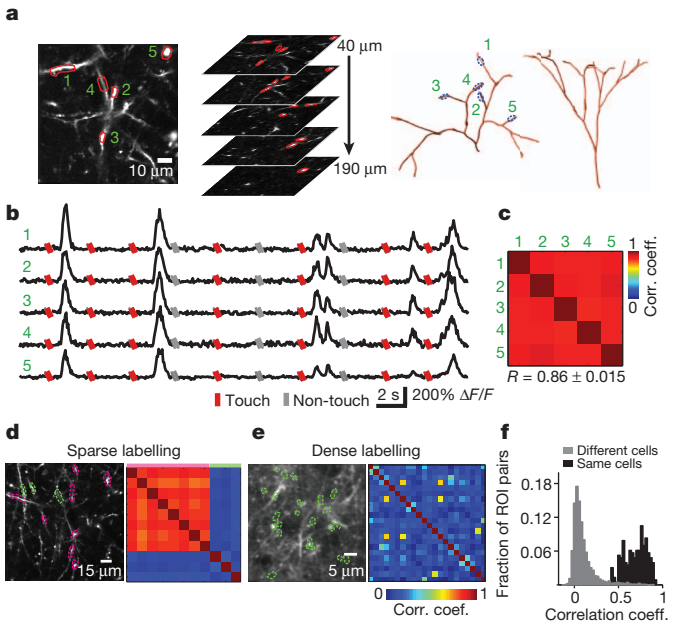


**Figure 2 | Global dendritic tuft $Ca^{2+}$ signals during active sensing.** **a**, Simultaneous $Ca^{2+}$ imaging during behaviour from multiple tuft branches (1–5) of the same cell, identified using three-dimensional reconstruction of imaging stacks. **b**, Ten consecutive trials from the five ROIs indicated in **a**. Signals 0.5 s before to 0.5 s after the sampling period are shown. Vertical bars indicate trial types. **c**, Correlation matrix for the ROIs in **a**. **d**, $Ca^{2+}$-signal correlation between branches for sparsely labelled imaging fields. ROIs from the same (magenta) and different (green) cells are labelled. **e**, Correlation similar to that in **d**, for a densely labelled imaging field. **f**, Histogram of population data showing distribution of pair-wise correlation for ROIs from multiple cells ($R = 0.097 \pm 0.13$) and for ROIs from single cells ($R = 0.69 \pm 0.13$).

2.23 ± 0.55 Hz; Supplementary Fig. 6) that were associated with large dendritic $Ca^{2+}$ signals (Fig. 3 and Supplementary Fig. 6).

Dual dendritic whole-cell recordings from layer 5 pyramidal neurons in acute neocortical slices revealed that apical trunk $Ca^{2+}$ spikes evoked by local current injection decreased in amplitude as they spread back into the tuft dendrites, producing events that were very similar in amplitude, duration and shape to the unpaired events observed *in vivo* (Fig. 3g and Supplementary Figs 6 and 7). Such unpaired events were not associated with substantial GCaMP-mediated tuft $Ca^{2+}$ signals (Supplementary Fig. 8). Pairing of the back-spread apical trunk $Ca^{2+}$ spikes with simultaneous tuft dendrite depolarization also increased their amplitude and duration to a similar extent to the spikes observed in the *in vivo* recordings (paired events; Fig. 3g and Supplementary Figs 6 and 7). Similar results were obtained when synaptic input was used to produce tuft depolarization (Supplementary Fig. 9).

In addition to increasing the amplitude and duration of individual tuft plateau potentials, the local depolarization also produced multiple or repetitive events during the current-injection period[23] (mean plateau interval: 209 ± 20 ms). Multiple plateau potentials further enhanced the amplitude and duration of the associated tuft $Ca^{2+}$ signals (Supplementary Fig. 6). The time course of the $Ca^{2+}$ signals in the anaesthetized mice covered a similar range to those observed during active sensation (Fig. 3f and Supplementary Fig. 6). Together, these data indicate that tuft dendritic $Ca^{2+}$ signals recorded during active sensation were produced by single or repetitive tuft plateau potentials evoked through an interaction between apical dendrite $Ca^{2+}$ spikes and coincident tuft dendrite depolarization. Importantly, this interaction enhanced the frequency and duration of the apical trunk $Ca^{2+}$ spikes (paired trunk events; Fig. 3g and Supplementary Figs 6, 8 and 9), providing a mechanism by which tuft depolarization can effectively influence action potential output.

What might be the source of apical tuft depolarization during behavioural conditions? It is known that the vibrissal motor cortex (vM1) provides a major excitatory input to layer 1 of barrel cortex[1,2,24], and that vM1 neurons code for whisking parameters during active sensing behaviour, with this activity being fed back through vM1 axons to layer 1 of S1 (refs 25–27). We reasoned that the excitatory input from vM1 to the distal dendritic regions of S1 layer 5 pyramidal neurons

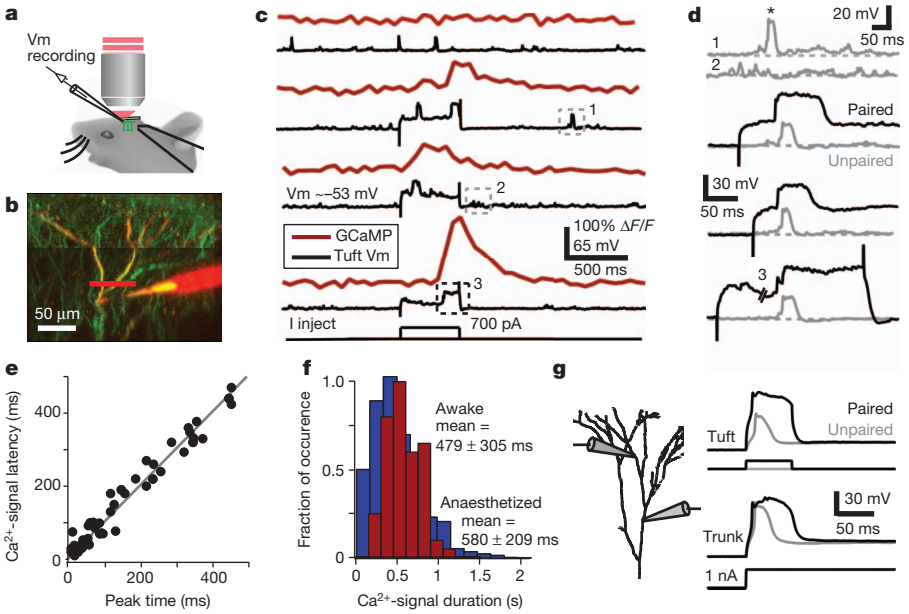


**Figure 3 | Dendritic $Ca^{2+}$ signals are produced by tuft plateau potentials.** **a**, Schematic of targeted dendritic patch-clamp recording from an anaesthetized mouse *in vivo*. Vm, membrane voltage. **b**, Side projection from a GCaMP3-expressing layer 5 pyramidal neuron. The pipette was filled with Alexa 594. **c**, $Ca^{2+}$ signals (red) and simultaneous intracellular voltage recordings (black). The top records contain only spontaneous dendritic voltage events without dendritic current injection. The three bottom records include 500-ms current injections. I inject, current injection. **d**, Detailed views of the voltage-recording traces in **c** (indicated by the dashed boxes). Top two traces show increased network activity that appears as excitatory postsynaptic potentials (EPSPs) and moderate unpaired events (asterisk). Bottom traces show that pairing of these spontaneous events (grey traces, unpaired) with tuft depolarization converts them into regenerative plateau potentials (black traces, unpaired). **e**, Tuft plateau potentials are highly correlated in time with $Ca^{2+}$ signals recorded nearby. **f**, Event-duration distributions for plateau-potential-evoked $Ca^{2+}$ signals from anaesthetized mice (red) and for all $Ca^{2+}$ events from awake behaving mice (blue). Occurrence normalized to maximum. **g**, *In vitro* simultaneous dual whole-cell voltage recordings from layer 5 pyramidal neuron tuft and apical trunk dendrites show that unpaired trunk spikes weakly spread into the tuft (grey trace), whereas those paired with local tuft depolarization become regenerative plateau potentials with enhanced amplitudes and durations (black trace).

may interact with ascending sensory input during active touch to produce the observed global distal dendritic nonlinearity. To test this, we silenced vM1 using localized muscimol injection and carried out calcium imaging from the same dendritic branches across several days of behavioural sessions. Dendritic $Ca^{2+}$ signals evoked by active touch during control sessions were largely abolished during sessions when vM1 was silenced, and recovered in subsequent recording sessions, approximately 24 h after injection (Fig. 4a, b, f and Methods). To control for the specificity of vM1 silencing, we injected the same dose of muscimol to a control site that was the same distance from the imaging window as vM1 (~3.2 mm). Imaging from the same dendritic branches showed that whisker touch-evoked dendritic $Ca^{2+}$ signals were still present after muscimol injection to the control site (Fig. 4a, b, g, h).

To determine the effect of vM1 silencing on whisker motion and the strength of sensory drive, we examined both whisking amplitude and the forces on the whiskers (total peak-curvature change ($|\Delta\kappa|$); see Methods) for each experimental condition. We found that vM1 silencing did not reduce the total $|\Delta\kappa|$ compared to the control condition (Fig. 4c), but it greatly diminished dendritic $Ca^{2+}$ signals for the entire range of sensory-input strength (Fig. 4e). Whisking amplitude

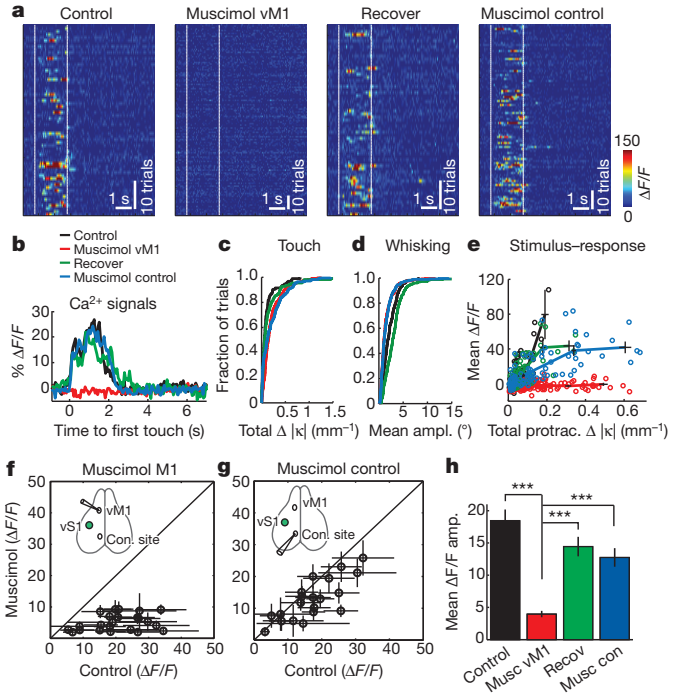


**Figure 4 | vM1 silencing abolished touch-evoked dendritic responses.** **a**, Colour raster of $Ca^{2+}$ signals of touch trials from a dendritic branch imaged across behavioural sessions for four conditions. White vertical lines indicate the sampling time. **b**, Averaged $Ca^{2+}$ signals aligned to the onset of whisker touch from all touch trials under each of the four conditions. **c**, Cumulative distribution of total peak-curvature change (total $\Delta|\kappa|$) for all touch trials under each of the four conditions. **d**, Cumulative distribution of mean whisking amplitude during sampling time for all touch trials under each of the four conditions. **e**, Stimulus–response relationship under each of the four conditions. Mean $\Delta F/F$ during sampling time plotted as a function of total $\Delta|\kappa|$ from protraction touch. Open circles, data from each trial. Solid lines connect binned data points. **f**, Summary of population data comparing $Ca^{2+}$ signals from the same dendritic branches during control sessions and sessions with muscimol injected into vM1 ($n = 23$ branches, 4 animals). **g**, Summary of population data comparing $Ca^{2+}$ signals from the same dendritic branches during control sessions and sessions with muscimol injected into a control site ($n = 20$ branches, 3 animals). **f**, Summary of population data of dendritic $Ca^{2+}$ signals under the four conditions. ***$P < 7 \times 10^{-7}$). Error bars, s.e.m.

during the sampling period was slightly reduced by muscimol injection to either vM1 or the control site (Fig. 4d). However, as dendritic responses were only affected by injection to vM1, this non-specific reduction in whisking amplitude cannot account for the reduced dendritic responses. We also observed that muscimol injection to vM1, but not to the control site, largely eliminated dendritic responses to a second type of whisker stimulation in awake animals (50-ms air puff; Supplementary Figs 4 and 10). These results indicate that distal tuft depolarization is required for the behaviourally evoked dendritic activity and that this depolarization is provided by vM1 input to L1. Thus, it seems that distal dendritic plateau potentials are responsible for producing a nonlinear dendritic integration of coordinated sensory and motor information in layer 5 pyramidal neurons during active sensing.

Finally, we observed a pronounced dependence of the dendritic $Ca^{2+}$ signal amplitude on the particular location of the whisker object touch (Fig. 5a, b). This location dependence does not seem to be due to differences in the mean forces generated by whisker touch at the different object locations (Fig. 5c). Furthermore, the relationship between dendritic response and whisker touch was found to vary as a function of the whisker angle during touch (set point: low-pass filtered whisker angle; Methods), even for similar touch force magnitude ranges (Fig. 5d). Grouped data from mice with a single whisker contacting the object at different locations revealed a marked tuning of the stimulus–response slope to particular whisker set-point locations (Fig. 5e). Thus, the variation in dendritic response amplitude at different object locations may be the result of a whisker angle set-point-dependent modulation of the stimulus–response slope or gain. Such an adjustable gain could be produced by whisker set-point-dependent variations in vM1 input to the tuft dendrites of layer 5 pyramidal neurons[26,27]. These data suggest that a circuit-level computation is implemented in the distal dendrites of layer 5 pyramidal neurons through the integration of correlated sensory and motor information during active touch to produce an object-localization signal.

Our current understanding of dendritic computation during behaviour is limited. Recent recordings from populations of pyramidal-neuron dendrites suggest an active role for dendrites in information processing during the awake state[21,28]. Here we report that novel long-duration plateau potentials and associated global dendritic $Ca^{2+}$ signals (Figs 2 and 3) are produced in the apical dendrites of individual layer 5 pyramidal neurons when mice perform an active sensing task. The $Ca^{2+}$-mediated dendritic plateau potentials were probably evoked by correlated perisomatic input from ascending sensory drive (Fig. 1) and layer 1 synaptic inputs from cortico–cortical feedback connections[1,26] (Fig. 4). This active input processing in pyramidal-neuron dendrites seems to underlie a circuit computation for the tactile localization of salient objects (Fig. 5 and Supplementary Fig. 12). Thus, our results suggest that active nonlinear dendritic integration in layer 5 pyramidal neurons has a central role in the production of a behaviourally related computation in the barrel cortex. Because pyramidal neurons throughout the central nervous system (CNS) are capable of producing related forms of active dendritic integration[7], the above correlation-based computations may be a common feature of many neuronal circuits[7–10,29,30].

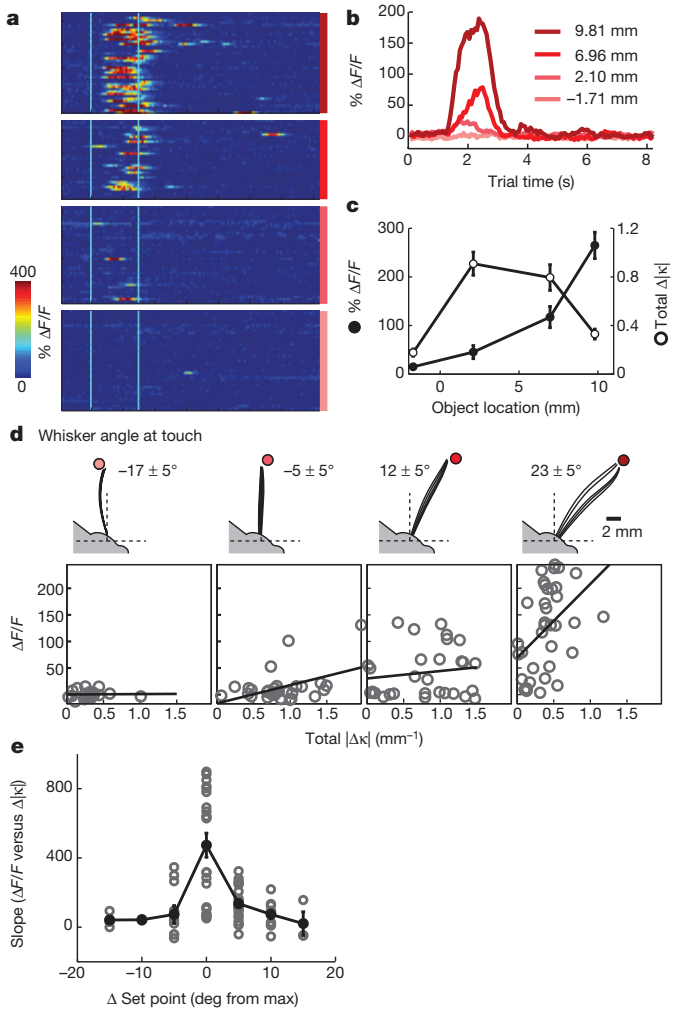


**Figure 5 | Whisker-angle dependence and object-location selectivity.** **a**, Colour raster of dendritic $Ca^{2+}$ signals from an example ROI. Trials are sorted according to object locations (indicated by red vertical bars, as shown in **b**). **b**, Mean $\Delta F/F$ averaged from trials with different object locations. Colours correspond to object locations (measured as the distance from the centre of the whisker pad along the anterior–posterior axis). **c**, Averaged $Ca^{2+}$ signals (filled circles) and total touch induced $|\Delta\kappa|$ (open circles) plotted against object location (object locations as above). **d**, Stimulus–response relationship for dendritic $Ca^{2+}$ signals at different object locations. Top row, projection of five frames of a tracked whisker showing whisker–object contact at different object locations (object locations as above). Whisker images were truncated beyond the object. Whisker set points at touch are indicated. Bottom row, $\Delta F/F$ during sampling time as a function of touch-induced total $|\Delta\kappa|$ for different object locations (whisker angles). Lines are linear regression fits. **e**, The slope of stimulus–response relation (from linear regression as in **d**) from trials binned by whisker set point during touch (bin size = 5°) for population data ($n = 22$ branches from 5 animals with single whisker–object contacts). Whisker set-point bins for all dendritic branches were aligned with the highest slope value set to 0°. The slope value at 0° is significantly higher than that obtained in the same manner from randomly permuted data ($P < 0.0001$; see Methods). Open grey circles indicate data from single dendritic ROIs, filled black circles represent averaging across all ROIs for each set-point bin (mean ± s.e.m).

## METHODS SUMMARY

The GCaMP3 (ref. 11) was expressed using a virus (rAAV-syn-GCaMP3, serotype 2/1, University of Pennsylvania Gene Therapy Program Vector Core), which was injected stereotactically into S1 (20 nl, 750 μm below pia) of adult C57BL/6 male mice (older than postnatal day 60 (P60)) and a circular craniotomy (1.5–2 mm) was made over the left S1. Animals were trained in a head-fixed whisker-based object-localization task. Distal apical dendrites from deep layer neurons were imaged using a custom two-photon microscope during task performance. Images of the whiskers were acquired using a high-speed CMOS camera (EoSense CL, Mikrotron) at 500 frames per s.

**Full Methods** and any associated references are available in the online version of the paper.

**Received 12 July 2011; accepted 19 September 2012.**
**Published online 11 November 2012.**

1. Cauller, L. J., Clancy, B. & Connors, B. W. Backward cortical projections to primary somatosensory cortex in rats extend long horizontal axons in layer I. *J. Comp. Neurol.* **390,** 297–310 (1998).
2. Petreanu, L., Mao, T., Sternson, S. M. & Svoboda, K. The subcellular organization of neocortical excitatory connections. *Nature* **457,** 1142–1145 (2009).

3. Larkum, M. E., Zhu, J. J. & Sakmann, B. A new cellular mechanism for coupling inputs arriving at different cortical layers. *Nature* **398,** 338–341 (1999).
4. Williams, S. R. & Stuart, G. J. Dependence of EPSP efficacy on synapse location in neocortical pyramidal neurons. *Science* **295,** 1907–1910 (2002).
5. Takahashi, H. & Magee, J. C. Pathway interactions and synaptic plasticity in the dendritic tuft regions of CA1 pyramidal neurons. *Neuron* **62,** 102–111 (2009).
6. Spruston, N. Pyramidal neurons: dendritic structure and synaptic integration. *Nature Rev. Neurosci.* **9,** 206–221 (2008).
7. Rao, R. P. & Ballard, D. H. Predictive coding in the visual cortex: a functional interpretation of some extra-classical receptive-field effects. *Nature Neurosci.* **2,** 79–87 (1999).
8. Engel, A. K., Fries, P. & Singer, W. Dynamic predictions: oscillations and synchrony in top-down processing. *Nature Rev. Neurosci.* **2,** 704–716 (2001).
9. Shadmehr, R., Smith, M. A. & Krakauer, J. W. Error correction, sensory prediction, and adaptation in motor control. *Annu. Rev. Neurosci.* **33,** 89–108 (2010).
10. Sommer, M. A. & Wurtz, R. H. Brain circuits for the internal monitoring of movements. *Annu. Rev. Neurosci.* **31,** 317–338 (2008).
11. Tian, L. *et al.* Imaging neural activity in worms, flies and mice with improved GCaMP calcium indicators. *Nature Methods* **6,** 875–881 (2009).
12. O'Connor, D. H. *et al.* Vibrissa-based object localization in head-fixed mice. *J. Neurosci.* **30,** 1947–1967 (2010).
13. Clack, N. G. *et al.* Automated tracking of whiskers in videos of head fixed rodents. *PLOS Comput. Biol.* **8,** e1002591 (2012).
14. de Kock, C. P. J. & Sakmann, B. Spiking in primary somatosensory cortex during natural whisking in awake head-restrained rats is cell-type specific. *Proc. Natl Acad. Sci. USA* **106,** 16446–16450 (2009).
15. Curtis, J. C. & Kleinfeld, D. Phase-to-rate transformations encode touch in cortical neurons of a scanning sensorimotor system. *Nature Neurosci.* **12,** 492–501 (2009).
16. O'Connor, D. H., Peron, S. P., Huber, D. & Svoboda, K. Neural activity in barrel cortex underlying vibrissa-based object localization in mice. *Neuron* **67,** 1048–1061 (2010).
17. Helmchen, F., Svoboda, K., Denk, W. & Tank, D. W. *In vivo* dendritic calcium dynamics in deep-layer cortical pyramidal neurons. *Nature Neurosci.* **2,** 989–996 (1999).
18. Jia, H., Rochefort, N. L., Chen, X. & Konnerth, A. Dendritic organization of sensory input to cortical neurons *in vivo. Nature* **464,** 1307–1312 (2010).
19. Chen, X., Leischner, U., Rochefort, N. L., Nelken, I. & Konnerth, A. Functional mapping of single spines in cortical neurons *in vivo. Nature,* (2011).
20. Varga, Z., Jia, H., Sakmann, B. & Konnerth, A. Dendritic coding of multiple sensory inputs in single cortical neurons *in vivo. Proc. Natl Acad. Sci. USA* **108,** 15420–15425 (2011).
21. Gentet, L. J., *et al.* Unique functional properties of somatostatin-expressing GABAergic neurons in mouse barrel cortex. *Nature Neurosci.* **15,** 607–612 (2012).
22. Larkum, M. E., Nevian, T., Sandler, M., Polsky, A. & Schiller, J. Synaptic integration in tuft dendrites of layer 5 pyramidal neurons: a new unifying principle. *Science* **325,** 756–760 (2009).
23. Williams, S. R. Encoding and decoding of dendritic excitation during active states in pyramidal neurons. *J. Neurosci.* **25,** 5894–5902 (2005).
24. Mao, T. *et al.* Long-range neuronal circuits underlying the interaction between sensory and motor cortex. *Neuron* **72,** 111–123 (2011).
25. Huber, D. *et al.* Multiple dynamic representations in the motor cortex during sensorimotor learning. *Nature* **484,** 473–478 (2012).
26. Petreanu, L. *et al.* Activity in motor-sensory projections reveals distributed coding in somatosensation. *Nature* (2012).
27. Hill, D. N., Curtis, J. C., Moore, J. D. & Kleinfeld, D. Primary motor cortex reports efferent control of vibrissa motion on multiple timescales. *Neuron* **72,** 344–356 (2011).
28. Murayama, M. *et al.* Dendritic encoding of sensory stimuli controlled by deep cortical interneurons. *Nature* **457,** 1137–1141 (2009).
29. Kleinfeld, D., Berg, R. W. & O'Connor, S. M. Anatomical loops and their electrical dynamics in relation to whisking by rat. *Somatosens. Mot. Res.* **16,** 69–88 (1999).
30. Dave, A. S. & Margoliash, D. Song replay during sleep and computational rules for sensorimotor vocal learning. *Science* **290,** 812–816 (2000).


**Supplementary Information** is available in the online version of the paper.

**Acknowledgements** We thank L. Tian and L. Looger for GCaMP3 constructs; J. Chandrashekar, N. Ryba and C. Zuker for GCaMP3 transgenic mice; W. Denk for comments on the manuscript; N. Clack, G. Myers, T. Zhao, V. Iyer, S. Peron and S. Drukmann for help with software and analysis; and L. Petreanu for help with experimental apparatus. S.R.W. is supported by the Australian research council (FT100100502) and Australian National Health and Medical Research Council (APP1004575).

**Author Contributions** N.-L.X., K.S. and J.C.M. conceived the project and designed the experiments. N.-L.X. performed all behavioural and chronic imaging experiments, and data analysis. M.T.H. and S.R.W. carried out all *in vitro* experiments. J.C.M. performed *in vivo* dendritic recording experiments. D.H., D.H.O. and K.S. designed behavioural apparatus and whisker data-analysis code. N.-L.X. and J.C.M. wrote the paper with comments from all authors.

**Author Information** Reprints and permissions information is available at www.nature.com/reprints. The authors declare no competing financial interests. Readers are welcome to comment on the online version of the paper. Correspondence and requests for materials should be addressed to J.C.M. (mageej@janelia.hhmi.org).

## METHODS

**Chronic imaging window.** All procedures were in accordance with protocols approved by the Janelia Farm Research Campus Institutional Animal Care and Use Committee or Queensland Brain Institute Institutional Animal Care and Use Committee. All animals used in awake behaving experiments were adult male (older than P60) C57BL/6Crl mice (Charles River). During surgery, mice were anaesthetized with isoflurane (~2% by volume in $O_2$; SurgiVet, Smiths Medical). A craniotomy (~2 mm in diameter) was made over the left barrel cortex. The dura was left intact. Virus-containing solution was slowly injected (20 nl per site, 3 to 4 sites per animal; depth ~700 μm) into the cortex. The injection system was comprised of a pulled glass pipette (broken and bevelled to 25–30 μm (outside diameter); Drummond Scientific, Wiretrol II Capillary Microdispenser) back-filled with mineral oil. A fitted plunger was inserted into the pipette and advanced to displace the contents using a hydraulic manipulator (Narashige, MO-10). Retraction of the plunger was used to load the pipette with virus. The injection pipette was positioned with a Sutter MP-285 manipulator. After injection, the craniotomy was covered with a double-layered glass coverslip[25,31], sealed in place with dental acrylic (Jet Repair Acrylic, Lang Dental Manufacturing). The double-layered glass was comprised of a 177–200-μm-thick glass coverslip (diameter ~1.5 mm) attached to a larger glass coverslip (diameter ~5 mm) using ultraviolet cured optical adhesives (Norland Optical Adhesives 61). A titanium head-post with an opening on the left side was attached to the skull with cyanoacrylate glue and dental acrylic to permit head fixation and two-photon imaging over the cranial window. Mice were allowed at least 7 days to recover before water restriction.

**Head-fixed mouse behaviour.** We designed a head-fixed active object-localization task with multiple target-object locations that require the mice to use active touch to determine the location of a pole, while providing a variety of stimuli to the whiskers (with different object locations). In each trial, the target object (a vertical pole) was presented randomly at either one of multiple 'go' positions or at a single 'no-go' position along the anterior–posterior axis on the right side of the mice (8–9 mm lateralized from the whisker pad). The go position was located within easy reach by whisking, and the location varied from trial to trial on the anterior–posterior axis, within a range of ~18 mm (~5 mm posterior to ~13 mm anterior to the centre of the whisker pad). The no-go position was in an anterior position, but within reach of the whiskers. Mice were trained to report the detection of an object at one of the go positions by licking a water port, and to report an object at the no-go position by withholding licking. Trained mice typically did not touch the object in the anterior no-go location. The trial began with a delay of 0.5~1 s before the pole started to ascend (time of ascent ~0.3 s) into the plane of the whiskers (Fig. 1a). The pole stayed in the whisker field for 1.5~2 s (the 'sampling' period) before starting to descend out of the whisker plane (time of descent ~0.5 s) followed by an 'answer' period (1.5~2 s) during which the mouse responds by licking or withholding licking. Correct no-go responses ('correct rejections') were not rewarded, and incorrect go responses ('misses') were not punished. Licks occurring within the answer period were recorded as go responses. Correct go responses ('hits') were rewarded with a drop of water (~8 μl). The trial was paused for 2 s to give the mouse time to drink. Incorrect no-go responses ('false alarms') led to a 'time-out' period in which the trial was paused for ~2–5 s. Licking during this time-out period triggered additional time-out periods. Licking outside of answer and time-out periods had no consequences.

Behavioural training began after the mice had restricted access to water for at least 7 days (1 ml per day). On days with behavioural sessions, mice generally obtained all water for the day during the session (approximately 1 ml). Food was available ad libitum. The weight and health of the mice were monitored daily. After training, mice learned to respond with licking to whisker–object contact regardless of the position of the pole (Supplementary Fig. 2).

The behavioural apparatus was mounted under a custom two-photon microscope equipped with a high-speed whisker-imaging system, and was controlled by an open-source software system (Z. Mainen and C. Brody) running on MATLAB (Mathworks) communicating with a real-time system (TDT and RTLinux). Imaging sessions started after the mice had completed the initial training and reached a performance criterion of 75% correct responses or $d' > 1.8$ (Supplementary Fig. 2a).

During behaviour, whiskers were illuminated with collimated light using a high-power light-emitting diode (LED) source (960 nm, Roithner) and condenser optics (Thorlabs). Images were acquired through a telecentric lens (×0.36, Edmund Optics) by a high-speed complementary metal-oxide semiconductor (CMOS) camera (EoSense CL, Mikrotron) running at 500 frames per s (480 × 352 pixels; resolution, 26 pixels per mm). Image acquisition was controlled by Streampix 3 (Norpix). Synchronization of behavioural trials and two-photon imaging frames was achieved using pulses sent from the real-time behaviour system.

**Two-photon calcium imaging from distal dendrites during behaviour.** The genetically encoded calcium indicator GCaMP3 (ref. 11) was expressed under the human synapsin 1 promoter after infection with recombinant adeno-associated virus (AAV, serotype 2/1; produced by the University of Pennsylvania Gene Therapy Program Vector Core), which was injected stereotaxically to deep layer in barrel cortex. For sparse labelling of layer 5 neurons with GCaMP3, AAV carrying floxed GCaMP3 was co-injected with a diluted AAV carrying Cre recombinase (~1:10,000–1:5,000). This approach reduces the cell density of GCaMP3-expressing neurons without compromising the expression level. Fifteen to twenty days after virus injection, mice began training on the tactile detection task and two-photon imaging sessions began after the criterion of 70% correct responses was reached (5–7 days after the training began). Sessions analysed here occurred between days 25 and 40 post infection.

GCaMP3 was excited at 925 nm (typically 20–40 mW at the back aperture) with a Ti:Sapphire laser (Mai Tai, Spectra Physics) and imaged through a Nikon ×16, 0.8-N.A. objective. Emission light passed through a 565 DCXR dichroic filter (Chroma Technology) and a ET525/70m-2p filter (Chroma Technology) and was detected by a GaAsP photomultiplier tube (10770PB-40, Hamamatsu). Images (512 × 128 pixels) were acquired at ~16 Hz using ScanImage software[32,33].

Subregions that contain primarily GCaMP-positive apical dendritic trunks (from layer 5 neurons) at the depth range of 20–400 μm, but not layer 2 or layer 3 somas, were used to image distal dendrite activity. A set of initial trials were usually used to identify imaging fields that show visually identifiable response (corresponding to $\Delta F/F > 10\%$) during the sampling period before a full imaging and behaviour session was initiated. Because of the broad horizontal extension of tuft dendrites, the imaging regions are usually in the proximity of, but not limited to, the barrels corresponding to the present whiskers (determined using intrinsic signal imaging). In our data, 23% of active dendrites show touch responses (we define active dendrites as those that show discernable increase in fluorescence during trials, whether this activity is related to touch or not; see Supplementary Figs 2 and 3). This is an overestimate of the fraction of the total population, as less than 30% (estimated by number of pixels) of all dendrites in a given field of view were active (that is, >70% did not show any detectable change in fluorescence; see Fig. 2e and Supplementary Fig. 2a, b). We did not include in our analysis any fields of view that contained only inactive dendrites (>50% of the examined fields). Thus, although our experiments were not designed to provide an unbiased estimate of the fraction of active dendrites, our sampling strategy suggests ~5% of all layer 5 dendrites showed touch-related $Ca^{2+}$ signals.

***In vivo* dendritic patch-clamp recording.** All animals used in this section of the study were adult male or female (older than P60) GCaMP3-expressing transgenic mice (Thy1, line 10, Charles Zuker, Janelia Farm Research Campus). The animals were surgically prepared as described above for the chronic imaging experiments, except that a half coverslip was used as an optical window and agar (~1%) was applied between the dura–brain surface and the coverslip[17]. In addition, a portion of the dura covering the open surface of the neocortex was either surgically removed or partially digested by collagenase treatment (1 mg $ml^{-1}$ applied to the dura using filter paper for 4 min followed by a 5-min wash with bovine serum albumin (BSA)) before the application of the optical window. Animals were maintained on ~1.5–2% isoflurane saturated with $O_2$ throughout the surgical and experimental session. The craniotomy was perfused with artificial cerebrospinal fluid (aCSF) (in mM: 125 NaCl, 25 $NaHCO_3$, 1.25 $NaH_2PO_4$, 3 KCl, 1.3 $CaCl_2$, 1.0 $MgCl_2$, 25 glucose) saturated with 95% $O_2$ and 5% $CO_2$. Whole-cell current-clamp recordings were made from tuft dendrites of thick-tufted layer 5 pyramidal neurons using a two-photon targeting method described below and a Dagan BVC-700 amplifier in 'bridge' mode, filtered at 1 kHz and digitized at 50 kHz. Pipettes had an open tip resistance of 7–10 MΩ when filled with (in mM): 134 K-gluconate, 6 KCl, 10 HEPES, 4 NaCl, 0.3 Tris2-GTP, 4 MgATP, 14 phosphocreatine, 0.05 Alexa 594. Pipette capacitance was neutralized just before seal formation and the bridge balance was typically 50–100 MΩ after break-in.

To target the distal dendrites of GCaMP-expressing layer 5 neurons, the anaesthetized mice were mounted to a head-fixation device under a custom two-photon microscope. GCaMP3 was excited at 900 nm (typically ~20 mW at the back aperture) with a Ti:sapphire laser (Chameleon Ultra II, Coherent) and imaged through a Nikon ×16, 0.8-N.A. objective. Emission light passed through a 565 DCXR dichroic filter (Chroma Technology) and a ET525/70m-2p filter (Chroma Technology) and was detected by a GaAsP photomultiplier tube (10770PB-40, Hamamatsu). Images (512 × 128 pixels) were acquired at either 8 or 16 Hz using ScanImage software. Dendrites were selected for recording based on their morphology (large-diameter dendritic trunk and extensive tuft arborization). To ensure the targeting of layer 5 dendrites, the trunk of the dendrite was traced with the two-photon microscope to a depth of at least 400 μm below the cortical surface. The two-photon microscope was used to target the recording pipette (filled with 50 μm Alexa 594) to secondary or tertiary branch points in the apical tuft. Once

in whole-cell mode, resting membrane potential was assessed (range: −55 to −49 mV) and various current steps (from 100 to 1,000 pA, 500 ms) were injected to evoke plateau potentials or calcium spikes (input resistance = 38 ± 0.3 MΩ; $n = 6$). During the current injections, $Ca^{2+}$ imaging was performed at ~16 Hz over ROIs that contained the recorded dendritic arborization as assessed by red fluorescence emission from the Alexa 594. Unpaired electrical events (events outside current injection periods) were selected for characterization using a threshold-level detection algorithm (threshold = 20 mV above baseline). Unpaired events and plateau potential (threshold = −20 mV) peak time, amplitude and duration, as well as $Ca^{2+}$-signal latency (interpolated time at which $\Delta F/F$ exceeded noise by 2 s.d.) peak amplitude and duration were automatically determined using a custom detection algorithm (Igor Por). Event durations are full width at half maximum for $Ca^{2+}$ signals or half width (electrical).

**Imaging data analysis.** Lateral motion in two-photon images recorded during behaviour was corrected in two steps (Supplementary Fig. 3b). All frames from a behavioural session were first aligned to a target image frame using an efficient cross-correlation-based registration algorithm (single-step discrete fourier transformation (DFT) algorithm)[34]. The target image was obtained by mean projection of image frames from a trial visually identified to contain still frames. After whole-frame alignment, within-frame motion artefacts were corrected with a line-by-line registration algorithm using the gradient-descent method[35].

For the data set from densely labelled dendrites with sparse signals, independent component analysis (ICA) was used to facilitate defining ROIs[36]. ICA was carried out using a published algorithm, FastICA[37], after dimensionality reduction using singular value decomposition on the data matrix from a fraction of trials (typically 50 trials) for each imaging field (each trial contains 128 frames with each frame containing 128 × 512 pixels). This method generated independent components with hot spots well matching dendritic branch structures that showed transients in sampled trials (Supplementary Fig. 3a, b). The number of independent components was empirically determined such that further increases in their number extracted only noise. ROIs were then manually outlined to include visually distinct hot spots. Because belonging to the same independent component does not necessarily mean belonging to the same dendritic branch or the same cell, multiple ROIs were often defined for the same independent component. This method of ROI selection was corroborated by an alternative approach using time projection of maximum value of pixel intensity above mean, $F_{max} - F_{mean}$, where $F$ is the time series of fluorescence intensity from each pixel. For each ROI, $\Delta F/F$ (%) was calculated as $(F - F_0) / F_0 \times 100$, where $F_0$ is the mode defined from the histogram of $F$. ROIs with clear spatial cross-talk were visually identified and excluded for analysis. ROIs typically showed two response types, with $Ca^{2+}$ signals occurring either during the whisker sampling epoch (during the presence of the pole; Fig. 1c) or in the post-sampling epoch (after the pole was removed from the whisker field, responses during this period were often less reliable and there was a lack of time locking to tractable behavioural variables; Supplementary Fig. 4).

To estimate the amplitude and duration of individual $Ca^{2+}$ transients during behavioural sessions, we used a simple events-detection approach, and measured the peak $\Delta F/F$ and full width at half maximum of identified $Ca^{2+}$ events. The events detection was based on combined thresholding with both amplitude (>4 standard deviation, estimated using median absolute deviation (MAD)) and rising slope (computed from a span of three frames) of $\Delta F/F$ time series from all trials of a given ROI. $Ca^{2+}$ transients during *in vivo* dendritic patch recording were visually identified, from which the amplitudes and durations were estimated. $Ca^{2+}$ events during behaviour sessions with a full width at half maximum of less than two frames (128 ms) were considered to be noise and were rejected.

For the analysis of active-sensing-related dendritic $Ca^{2+}$ signals (Fig. 1c–e), only ROIs selective to sampling epoch (compared to the post-sampling epoch, $P < 0.05$, Wilcoxon rank-sum test) were used, and ROIs from the same independent components showing strong correlation with each other were treated as redundant, and only one of these was used. For the analysis of signal correlation between branches (Fig. 2a–d and Supplementary Fig. 9), ROIs were included regardless of their trial epoch selectivity, and for a given branch, only one ROI was included. For signal correlation in single cells, ROIs were from sparsely labelled imaging fields in which branches could be traced to single apical trunks, and reconstructed (Fig. 2a) with the custom-written software neuTube[38] using imaging stacks (512 × 512 resolution, 1 μm per slice) acquired with a two-photon microscope at the end of each experiment. For signal correlation under densely labelled conditions, branches in a small field of view are likely to originate from many different cells, and ROIs from branches were included regardless of their origin. For the whisker set-point dependence of the stimulus-response relation shown in Fig. 5e, we controlled for potential bias introduced by the alignment of the maximum value to 0° by randomly permuting the data points for each ROI into 4 bins. A paired $t$-test was used to compare the maximum slope values from these randomly permuted data bins with the maximum slope values from the data binned by set point as in Fig. 5e. The maximum slope value shown in Fig. 5e is significantly different to those obtained from randomly permuted data ($P < 0.0001$).

Details of the method for extracting whisker variables have been described previously[12,13]. In brief, the whisker angle at the base of the whisker, θ, was extracted from tracked whisker trajectories. A line perpendicular to the midline was defined as θ = 0 and protraction corresponded to increasing angles. Whisking set point is the low-pass (<6 Hz) filtered whisker-angle time series [θ(t)], capturing mainly temporally averaged whisker positions. The amplitudes of the forces in the follicle are proportional to the curvature of the whisker. We used curvature change (Δκ; Fig. 1a) at a particular location along the whisker (2–3 mm) as a substitute for the mechanical forces acting on the whiskers. Curvature was determined using a second-order polynomial fit to the whisker backbone. Automatic detection of whisker–pole contact was based on thresholding Δκ with the standard deviation estimated using MAD from frames with a minimal whisker–pole distance for at lease three consecutive frames (6 ms; Fig. 1a). The total curvature change during contacts, which was used as a metric for overall touch-evoked sensory drive in a given trial, is computed by summation of the absolute value of peak Δκ for each contact period. Unless otherwise indicated, data in the text are reported as mean ± s.d.

**Passive whisker stimulation.** Compressed air was delivered through a glass pipette pointing towards a single whisker (C2) near the tip. An air puff to the whiskers during the anaesthetized condition is ineffective in evoking any dendritic response (Supplementary Fig. 10). Air puff during the awake condition occasionally evoked dendritic responses. Dendrites often show a distinct response to air puff compared to active touch, with a lower threshold response to active touch (Supplementary Fig. 10d, e). A small fraction (6%) of dendritic branches responded to both air puff and active touch (Supplementary Fig. 10f). To control for the potential spread of air puff to the whisker pad and the animal's face, the whiskers were trimmed at the end of experiments, and the air puff was directed towards the face. The same dendrites that had showed a response to air puff directed at the whiskers did not show any detectable responses to air puff directed at the whisker pad or face (data not shown).

**Reversible silencing.** To reversibly silence vM1, the GABA (γ-aminobutyric acid) agonist muscimol hydrobromide (Sigma-Aldrich) was dissolved in saline (5 μg $\mu l^{-1}$), and 60 nl were injected slowly (10 nl per min) to vM1 (1.1 mm lateral to midline and 0.9 mm anterior to Bregma, depth 550–600 μm under the pia) of the ipsilateral side of the S1 imaging window[25]. For control-site injection, the same dose of muscimol was injected to a control cortical area of the same hemisphere with the distance to the centre of imaging window the same as that for M1 injection (1.1 mm lateral, 3.4 mm posterior to Bregma, depth 550–600 μm). The animals were left to recover for 2 h before the behavioural session. To test the possibility that the feedback from motor cortex to S1 is also required for air-puff-evoked dendritic response during the awake condition, dendritic calcium imaging with air-puff stimulation was also conducted on the day of muscimol injection to either M1 or to the control site. M1 silencing led to dropped task performance, but the animal drank normally when water was freely available, suggesting that M1 inactivation did not impair licking function.

***In vitro* slice preparation and patch-clamp recording.** Under control conditions, recordings were made from layer 5B pyramidal neurons visualized in near-coronal brain slices (300 μm) of the somatosensory neocortex prepared from Wistar rats (4–8 weeks old). Slices were perfused with a solution of composition (mM): 125 NaCl; 25 $NaHCO_3$; 3 KCl; 1.25 $NaH_2PO_4$; 2 (or 1.3) $CaCl_2$; 1 $MgCl_2$, 3 Na pyruvic acid and 25 glucose at 35 to 37 °C bubbled with 95% $O_2$ and 5% $CO_2$. Dual whole-cell recordings were made with identical current-clamp amplifiers (BVC-700A; Dagan Corporation). Pipettes were filled with (mM) 135 K-gluconate; 7 NaCl; 10 HEPES; 2 $Na_2$-ATP; 0.3 Na-GTP; 2 $MgCl_2$ and 0.01 Alexa Fluor 568 (Molecular Probes, Eugene) (pH 7.3–7.4; KOH) and had open-tip resistance of 8–12 MW. Current and voltage signals were low-pass filtered (DC to 10 KHz) and acquired at 30–50 kHz. Data were acquired and analysed using AxographX software (AxographX). For each neuron, the apical dendritic recording pipette was positioned as close as possible to the nexus of the apical dendritic trunk (21 ± 9 mm, $n = 13$) and a second pipette positioned at an apical dendritic tuft site under infrared differential interference microscopy. At the termination of each whole-cell recording, the location of recording pipettes and neuronal morphology was examined by fluorescence microscopy and digitally recorded (Retiga EXI, QImaging).

For *in vitro* recordings from GCaMP-expressing layer 5 pyramidal neurons, acute coronal slices containing the barrel and/or somatosensory cortices were prepared from 4–7-week-old male wistar rats (Charles River, OGB-6F experiments) or from 6–8-week-old male wistar rats injected with GCaMP3 virus at 3–3.5 weeks of age. Animals were deeply anaesthetized with isoflurane saturated with $O_2$ and decapitated; the brain was rapidly removed and sectioned at 300 μm with a Leica VT1200S vibrating tissue slicer in ice-cold slicing aCSF (in mM:

125 NaCl, 25 $NaHCO_3$, 1.25 $NaH_2PO_4$, 3 KCl, 1.0 $CaCl_2$, 5.0 $MgCl_2$, 25 glucose, 3 pyruvate, 1 ascorbate) saturated with 95% $O_2$ and 5% $CO_2$. Slices recovered at 34 °C for 20–30 min and were subsequently stored at room temperature (20–25 °C) until use. Whole-cell current-clamp recordings were made from thick-tufted layer 5 pyramidal-neuron distal apical trunks or primary tuft dendrites using conventional dodt optics with a Dagan BVC-700 amplifier in 'bridge' mode, filtered at 1–5 kHz and digitized at 50 kHz. Experiments were performed at 34–37 °C in aCSF containing (in mM): 125 NaCl, 25 $NaHCO_3$, 1.25 $NaH_2PO_4$, 3 KCl, 1.3 $CaCl_2$, 1.0 $MgCl_2$, 25 glucose, 3 pyruvate, 1 ascorbate. Pipettes had an open tip resistance of 4-6 MΩ when filled with (in mM): 134 K-gluconate, 6 KCl, 10 HEPES, 4 NaCl, 0.3 Tris2GTP, 4 $Mg_2ATP$, 14 phosphocreatine, 0.05 Alexa 594. After pipette capacitance neutralization and bridge balance (typically between 12 and 24 MΩ after break-in, experiments were terminated if series resistance (Rs) exceeded 40 MΩ) current steps were injected to characterize basic response properties. Dendrites were only accepted for recording if they exhibited prominent h-current sag (H-sag; 40–80%), a resting membrane voltage of more negative than −53 mV, and a short-latency, rapidly rising voltage spike that crossed 0 mV in response to large depolarizing current injection ('plateau potentials' or 'calcium spikes', rheobase of 0.8 to 2.0 nA). All patched dendrites were confirmed to originate from intact somas in layer 5. Synaptic stimulation was carried out in the presence of 2.5 μM GABAzine (SR95331) with a bipolar stimulating electrode placed in layer 1 (~50–100 μm below the pia and ~200–400 μm lateral to the dendritic patch pipette). Each synaptic stimulation experiment imaged at least two separate branches to confirm widespread back-propagation of the plateau potential.

***In vitro* two-photon imaging and uncaging.** Two-photon imaging and uncaging was carried out using a dual galvanometer-based scanning system (Prairie Technologies) coupled with two pulsed, ultra-fast Ti:sapphire lasers (Chameleon Ultra II, Coherent) with their intensity controlled separately by two electro-optical modulators (Conoptics). Alexa 594 was excited at 880 nm to visualize morphology while OGB-6F (100 μM) and GCaMP3 were excited at 92 nm with line-scans through dendrites of interest at high magnification with dwell times of 8–12 μs at 150–500 Hz. GCaMP3 and OGB-6F signals are expressed as $\Delta F/F$ (%) (calculated as $((F - F_{baseline}) / F_{baseline}) \times 100$). Between 3 and 12 individual line-scans were averaged for each condition. Care was taken to collect data only from dendrites that were at least 30 μm (and up to 150 μm) below the surface of the slice that were not prematurely cut off before termination: we consistently observed morphological abnormalities and significantly higher resting $\Delta F/F$ along with substantial plateau-evoked GCaMP or OGB-6F signals in branches that did not meet these criteria (data not shown), presumably owing to the effects of structural damage on their electrotonic architecture. Branches were anatomically defined as incrementing from 0° at the apical trunk. For fast, multi-site glutamate uncaging, 10 mM MNI-glutamate or 1–5 mM RUBI-glutamate (Tocris; dissolved in aCSF) was delivered via pressure ejection through a specially designed puffer pipette to the surface of the slice while focused 720-nm (MNI) or 800-nm (RUBI) laser light was rapidly directed to a sequence of pre-selected points near spine heads (10–20 points over 20–30 μm, 0.2 ms dwell time, 0.1 ms move time).


31. Komiyama, T. *et al.* Learning-related fine-scale specificity imaged in motor cortex circuits of behaving mice. *Nature* **464,** 1182–1186 (2010).
32. Pologruto, T. A., Sabatini, B. L. & Svoboda, K. ScanImage: flexible software for operating laser scanning microscopes. *Biomed. Eng. Online* **2,** 13 (2003).
33. Iyer, V. *et al. ScanImage for* in vivo *laser scanning microscopy* Program No. 485.2. 2009 Neuroscience Meeting Planner (Society for Neuroscience, 2009).
34. Guizar-Sicairos, M., Thurman, S. T. & Fienup, J. R. Efficient subpixel image registration algorithms. *Opt. Lett.* **33,** 156–158 (2008).
35. Greenberg, D. S. & Kerr, J. N. D. Automated correction of fast motion artifacts for two-photon imaging of awake animals. *J. Neurosci. Methods* **176,** 1–15 (2009).
36. Mukamel, E. A., Nimmerjahn, A. & Schnitzer, M. J. Automated analysis of cellular signals from large-scale calcium imaging data. *Neuron* **63,** 747–760 (2009).
37. Hyvärinen, A. & Oja, E. Independent component analysis: algorithms and applications. *Neural Netw.* **13,** 411–430 (2000).
38. Zhao, T. *et al.* Automated reconstruction of neuronal morphology based on local geometrical and global structural models. *Neuroinformatics* **9,** 247–261 (2011).